Nano Research

Open Access

Research Article

Cationic defect-enabled charge transfer in rhodium clusters via Rh–O bonding for enhanced alkaline hydrogen evolution

Qingao Li[1,2], Huanhuan Zhang[2], Dian Yang[2], Junjie Gong[2], LiLi Zhang[2], Lin Gu[3], Shichang Chen[1] ✉, Shijie Shen[2,4] ✉, and Wenwu Zhong[2,5] ✉

[1] *School of Materials Science, Engineering, Zhejiang Sci-Tech University, Hangzhou 310018, China*
[2] *Zhejiang Key Laboratory for Island Green Energy and New Materials, Taizhou University, Taizhou 318000, China*
[3] *Beijing National Center for Electron Microscopy and Laboratory of Advanced Materials, Department of Materials Science and Engineering, Tsinghua University, Beijing 100084, China*
[4] *ERA Co., Ltd., Taizhou 318020, China*
[5] *School of Chemistry and Chemical Engineering, Shaoxing University, Shaoxing 312000, China*

Cite this article: *Nano Research*, **2025**, *18*, 94907391. https://doi.org/10.26599/NR.2025.94907391

ABSTRACT: Rhodium (Rh)-based catalysts have shown superior potential over platinum for the alkaline electrocatalytic hydrogen evolution reaction (HER). However, achieving high catalytic activity while minimizing Rh usage remains a significant challenge. Herein, we anchored 1.48 wt.% Rh clusters onto nickel-iron layered double hydroxides with cationic defects. The Rh clusters exhibit multiple highly reactive crystallographic facets, providing numerous active sites for catalytic reactions. The cationic vacancies facilitate efficient charge transfer between the Rh clusters and the support through Rh–O bonds, lowering the d-band center of Rh and optimizing hydrogen adsorption strength. Consequently, the synthesized catalyst demonstrates exceptional performance, achieving an ultra-low overpotential of 4 mV at 10 mA·cm^{-2}, surpassing all previously reported Rh-based catalysts. This work presents a promising strategy for designing cost-effective and highly efficient alkaline HER catalysts.

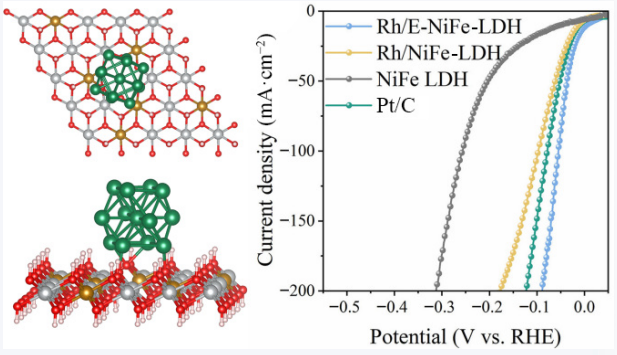

KEYWORDS: Rh clusters, cationic defects, nickel-iron layered double hydroxide (NiFe-LDH), electrocatalyst, hydrogen evolution reaction (HER)

1 Introduction

Hydrogen energy has emerged as a cornerstone in the global transition toward a clean, sustainable, and carbon-neutral energy future. Among various hydrogen production methods, water electrolysis stands out as a clean and scalable approach for generating high-purity hydrogen [1–3]. However, the efficiency of water electrolysis is inherently limited by the sluggish kinetics of the hydrogen evolution reaction (HER), which involves multiple proton-coupled electron transfer steps [4]. While HER in acidic media has been extensively optimized, HER in alkaline media remains particularly challenging due to the additional energy barrier associated with water dissociation [5–7]. This has spurred significant research into developing advanced catalysts that can drive HER efficiently under alkaline conditions [8–11], with a focus on reducing overpotential, improving catalytic kinetics, and ensuring long-term stability in corrosive alkaline environments.

Based on a wealth of experimental investigations and density functional theory (DFT) calculations [12, 13], platinum (Pt) is widely regarded as the optimal catalyst for HER in acidic solutions due to its near-zero overpotential and exceptional catalytic kinetics [14, 15]. However, Pt's performance in alkaline electrolytes is significantly reduced, exhibiting catalytic activity two orders of magnitude lower than in acidic conditions [16]. This decline is primarily attributed to the sluggish kinetics of water dissociation in alkaline conditions, which limits the availability of hydrogen intermediates at the catalytic surface. In contrast, rhodium (Rh), another Pt group element, exhibits a much smaller discrepancy in catalytic activity between acidic and alkaline media, with only a one-

Received: January 27, 2025; **Revised:** March 18, 2025
Accepted: March 19, 2025

✉Address correspondence to Shichang Chen, scchen@zstu.edu.cn; Shijie Shen, shensj@tzc.edu.cn; Wenwu Zhong, zhongww@tzc.edu.cn

order-of-magnitude difference [17]. Furthermore, several Rh-based catalysts have demonstrated catalytic activity in alkaline electrolytes that rivals or even surpasses that of Pt [18–22]. These unique attributes make Rh-based catalysts highly promising for HER in alkaline environments, offering both high activity and superior adaptability across different pH conditions. Notwithstanding these benefits, the extensive utilisation of Rh is obstructed by two significant challenges: (i) its pricey cost and scarcity, which limit economic feasibility and (ii) its strong hydrogen adsorption, which impedes the desorption step and negatively affects overall reaction kinetics. Therefore, developing strategies to enhance Rh utilization and reduce its hydrogen adsorption strength remains a crucial focus in designing advanced HER catalysts.

One promising approach to address these challenges is to load Rh in the form of single atoms, nanoclusters, or nanoparticles onto a suitable support material that can stabilize the Rh species, prevent agglomeration, and modulate their electronic structure [23–25]. Nickel-iron layered double hydroxide (NiFe-LDH), an earth-abundant and low-cost material, has gained attention due to its layered structure, excellent stability in alkaline media, and tunable electronic properties [26–28]. The synergistic interaction between Ni and Fe atoms in NiFe-LDH promotes electron transfer and enhances the adsorption of reactant species, contributing to its catalytic activity [29, 30]. Additionally, the layered structure of NiFe-LDH provides abundant active sites and accelerates mass and charge transport, making it an ideal support material for noble metal catalysts [31–33]. The integration of Rh onto NiFe-LDH has been shown to significantly enhance HER performance by leveraging the complementary properties of both materials [34–37]. However, despite these advances, challenges remain in achieving high activity while minimizing the amount of Rh used.

In this study, we synthesized Rh clusters supported on NiFe-LDH with cations vacancies and evaluated their performance for electrocatalytic hydrogen evolution in alkaline media. The Rh clusters expose multiple crystal planes, each of which contributes to high hydrogen evolution activity. The incorporation of cation vacancies negatively shifts the d-band center of Rh while simultaneously enhancing the conductivity and charge transfer characteristics of the catalyst, leading to a synergistic improvement in HER performance. The resulting catalyst achieves an ultra-low overpotential of 4 mV at 10 $mA{\cdot}cm^{-2}$, with a mass activity at −100 mV (vs. reversible hydrogen electrode (RHE)) that is 25.7 times greater than that of conventional Pt/C catalysts. This work provides a general framework for the rational design of advanced catalysts through defects engineering and noble metal integration.

2 Experimental methods

2.1 Synthesis of Rh/etched NiFe-LDH (E-NiFe-LDH)

Rh/NiFeZn-LDH was synthesized on a three-dimensional nickel foam substrate via a one-pot solvothermal method. The precursor solution was prepared by dissolving 0.75 mmol $Ni(NO_3)_2{\cdot}6H_2O$, 0.6 mmol $Fe(NO_3)_3{\cdot}9H_2O$, 0.15 mmol $Zn(NO_3)_2{\cdot}6H_2O$, 1.4 mmol hexadecy trimethyl ammonium bromide (CTAB), and 0.15 mmol $RhCl_3{\cdot}xH_2O$ in a mixed solvent of 36 mL methanol and 6 mL deionized water, followed by vigorous stirring until complete dissolution. Prior to synthesis, a nickel foam substrate (2 cm × 3 cm) was sequentially cleaned with acetone, 1 M hydrochloric acid, deionized water, and ethanol to remove surface contaminants. The cleaned nickel foam was then vertically immersed in the precursor solution within a 50 mL Teflon-lined stainless-steel autoclave. The solvothermal reaction was conducted at 180 °C for 24 h in an oven. After natural cooling to room temperature, a uniform brown layer was observed on the nickel foam surface. The resulting product, designated as Rh/NiFeZn-LDH, was ultrasonically cleaned with water and methanol for 3 min and dried at 60 °C overnight. For alkaline etching, the catalyst was treated in 5 M KOH solution under continuous stirring at 60 °C for 6 h, yielding Rh/E-NiFe-LDH, which was subsequently washed with deionized water and ethanol. To investigate the effect of Rh content, additional samples were prepared using varying concentrations of $RhCl_3{\cdot}xH_2O$ (0.05, 0.1, and 0.2 mmol). Furthermore, a series of alkaline-etched samples were synthesized using different alkaline solutions (NaOH and KOH) with concentrations ranging from 4 to 6 M. The influence of cation defects was examined by controlling the etching duration (3 and 9 h) under identical conditions.

2.2 Synthesis of E-NiFe-LDH

E-NiFe-LDH was synthesized following an identical procedure to that of Rh/NiFeZn-LDH, with the exception of omitting the $RhCl_3{\cdot}xH_2O$ precursor from the reaction mixture.

2.3 Synthesis of Rh/NiFe-LDH

The synthesis procedure for Rh/NiFe-LDH paralleled that of E-NiFe-LDH, with the exceptions that alkaline etching was unnecessary, $Zn(NO_3)_2{\cdot}6H_2O$ was omitted, and 0.75 mmol $Ni(NO_3)_2{\cdot}6H_2O$ was substituted with 0.9 mmol $Ni(NO_3)_2{\cdot}6H_2O$.

2.4 Synthesis of NiFe-LDH

NiFe-LDH was synthesized following an analogous procedure to Rh/NiFe-LDH, with the sole modification being the exclusion of the $RhCl_3{\cdot}xH_2O$ precursor from the reaction mixture.

2.5 Synthesis of X/E-NiFe-LDH (X = Ir, Ru, and Pt)

The $RhCl_3{\cdot}xH_2O$ precursor was systematically replaced with equivalent molar concentrations of alternative Pt group metal chlorides, including $PtCl_4$, $RuCl_3$, and $IrCl_3$ while maintaining identical synthesis conditions.

2.6 Characterizations

The crystal structure of the synthesized materials was characterized by X-ray diffraction (XRD) measurement using a Rigaku D/MAX 2500 diffractometer with Cu Kα radiation (λ = 1.5418 Å). Morphological analysis was performed using field-emission scanning electron microscopy (FE-SEM, Hitachi S4800) measurement. Transmission electron microscopy (TEM) and energy-dispersive X-ray spectroscopy (EDX) mapping images were conducted on an FEI Talos F200X microscopy, with samples prepared by ultrasonic dispersion in ethanol followed by drop-casting onto carbon-coated copper grids. Raman spectroscopy measurements were obtained using a Horiba LabRAM HR Evolution spectrometer with 532 nm laser excitation. X-ray photoelectron spectroscopy (XPS) measurement was performed on a Thermo Scientific K-Alpha spectrometer, with all binding energies calibrated against the adventitious carbon peak at 284.8 eV. Electron paramagnetic resonance (EPR) spectra were recorded on a Bruker EMXplus-6/1 spectrometer at room temperature. Quantitative elemental analysis was carried out by inductively

coupled plasma optical emission spectrometry (ICP-OES) using a Thermo Fisher iCAP PRO instrument.

2.7 Electrochemical measurement for HER

Electrochemical measurements were conducted using a standard three-electrode configuration connected to a CHI 760e electrochemical workstation. The working electrode was prepared by depositing the synthesized catalyst onto nickel foam with a geometric surface area of 0.5 cm^2. A graphite rod and Ag/AgCl electrode served as the counter and reference electrodes, respectively. All potentials were converted to the RHE scale using the Nernst equation: $E_{RHE} = E_{Ag/AgCl} + 0.059pH + 0.197$ V and were *iR*-corrected (95%) to compensate for solution resistance, where E_{RHE} is electrode potential converted to the RHE potential and $E_{Ag/AgCl}$ is electrode potential measured against an Ag/AgCl reference electrode. For comparative analysis, a control electrode was prepared by depositing 20 wt.% Pt/C catalyst onto nickel foam under identical conditions. HER performance was evaluated through linear sweep voltammetry (LSV) measurements in 1 M KOH electrolyte (pH = 14) at a scan rate of 5 $mV \cdot s^{-1}$. Tafel slopes were derived from the corresponding polarization curves using linear fitting analysis. Electrochemical surface characteristics were investigated by cyclic voltammetry (CV) measurements within a potential window of −0.15 to −0.25 V (vs. RHE) at varying scan rates (20–100 $mV \cdot s^{-1}$). Electrochemical impedance spectroscopy (EIS) measurements were performed across a frequency range of 100 kHz to 0.1 Hz. The long-term stability was assessed through chronopotentiometry at a constant current density of 100 $mA \cdot cm^{-2}$. Post-stability characterization of the working electrode was conducted using XRD, SEM, TEM, and XPS measurements to evaluate structural and compositional changes.

2.8 DFT calculation methods

All of the computations were carried out using the Vienna *ab initio* simulation package (VASP) and the spin-polarized DFT using the projector augmented plane-wave approach. Perdew–Burke–Ernzerhof (PBE) generalized gradient approximation (GGA) was chosen for the exchange-correlation potential. The DFT-D3 method described the long-range van der Waals interaction. 480 eV was the fixed cut-off energy for plane waves. When solving the Kohn–Sham equation iteratively, the energy criterion was set at 10–5 eV. The remaining forces on the atoms were reduced to less than 0.02 $eV \cdot Å^{-1}$ by relaxing all the structures. VASPKIT and visualization for electronic and structural analysis (VESTA) were used for data processing and visualization. To avoid interlaminar interactions, a vacuum spacing of 20 Å was applied perpendicular to the slab. The charge density difference of the A/B heterostructure was defined as $\Delta\rho = \rho_{A+B} - \rho_A - \rho_B$, where ρ_{A+B}, ρ_A, and ρ_B represent the charge densities of A/B heterostructure, isolated A slab, and isolated B slab, respectively. The charge transfer quantity was expressed using the Bader charge. The Gibbs free energy (ΔG) for intermediates in HER was calculated as $\Delta G = \Delta E + \Delta E_{ZPE} - T\Delta S + \Delta G_U$, where ΔE represents the overall energy difference between the slab and respective terminations derived using DFT-PBE. $T\Delta S$ and ΔE_{ZPE} represent the entropy and zero-point energy differences between the gap phase and the adsorbed states of chemical intermediates, respectively. T stands for room temperature (298.15 K). U is the electrode potential, and $\Delta G_U = -eU$.

3 Results and discussion

3.1 Synthesis and structure characterization

Figure 1(a) illustrates the synthesis process of Rh clusters anchored on NiFe LDH with cationic vacancies (Rh/E-NiFe-LDH). Initially, Rh/NiFeZn-LDH was grown on a three-dimensional nickel foam skeleton using a one-pot solvothermal approach. Subsequently, the Zn component was selectively etched away using a potassium hydroxide solution. By carefully controlling the etching time and Rh content, Rh/E-NiFe-LDH was successfully synthesized. For comparative analysis, control samples, including Rh/NiFe-LDH, E-NiFe-LDH, and NiFe-LDH, were also prepared. XRD patterns were used to elucidate the crystal structure. The diffraction peaks at 44.5°, 51.8°, and 76.4° correspond to the nickel foam substrate (JCPDS No. 04-0850), as shown in Fig. S1 in the Electronic Supplementary Material (ESM). No distinct peaks attributable to the LDH phase were observed, which may be due to the amorphous nature of the LDH or the overwhelming intensity of the nickel foam peaks. Furthermore, the XRD pattern does not exhibit prominent peaks for Rh nanoparticles or Rh_2O_3, which suggests that Rh is likely present in the form of nanoclusters or potentially single atoms, a conclusion that will be further confirmed by high-resolution TEM (HR-TEM) measurement. The SEM image of Rh/NiFeZn-LDH displays evenly interconnected ultrathin two-dimensional nanosheets with a smooth surface (Fig. 1(d) and Fig. S2 in the ESM), which is attributable to the influence of cationic surfactants [38]. After etching for varying durations, the morphology of the catalyst retains its sheet-like configuration. Notably, the Rh/E-NiFe-LDH sample etched for 6 h demonstrates a distinctly roughened surface. Therefore, subsequent characterizations of the Rh/E-NiFe-LDH sample refer to those etched for 6 h if not specifically stated. In Fig. 1(b), HR-TEM image shows the presence of numerous small Rh clusters dispersed throughout the sample at varying distances and orientations. The blue dashed box indicates the Rh (111) crystal plane, the red dashed box highlights the Rh (200) plane, and the yellow dashed box corresponds to the Rh (220) plane. Other regions show no observable lattice fringes, which suggests that the NiFe-LDH portion is amorphous. Figure 1(c) provides magnified views of these Rh clusters. Further analysis reveals that the Rh clusters exhibit an average size of 3.51 nm (Fig. S3 in the ESM), which is known to enhance the density of active sites [39–41]. The selected area electron diffraction (SAED) pattern in Fig. 1(e) clearly identifies the Rh (111), Rh (200), and Rh (311) crystal planes, further confirming the presence of Rh nanoclusters and amorphous NiFe-LDH, as discussed previously. Figure 1(f) presents the Raman spectra of the samples. The pronounced peaks at 433 and 514 cm^{-1} are indicative of Ni–OH and Ni–O coupling vibrations, respectively [42]. A characteristic peak at 584 cm^{-1} in Rh/E-NiFe-LDH corresponds to the presence of cation vacancies [42], confirming the successful formation of vacancies through the alkaline etching process. Additionally, EPR spectroscopy was utilized to investigate cation defects within the material system. The Rh/E-NiFe-LDH sample exhibits a characteristic signal at g = 2.02 (Fig. S4 in the ESM), providing definitive evidence for the presence of cationic vacancies [43]. This approach aligns with established methodologies in Refs. [43–45], where cationic vacancies in NiFe-LDH are typically introduced by substituting partial Ni with divalent Zn or partial Fe with trivalent Al, followed by alkaline etching to remove Zn or Al, thereby generating Ni or Fe vacancies. The experimental

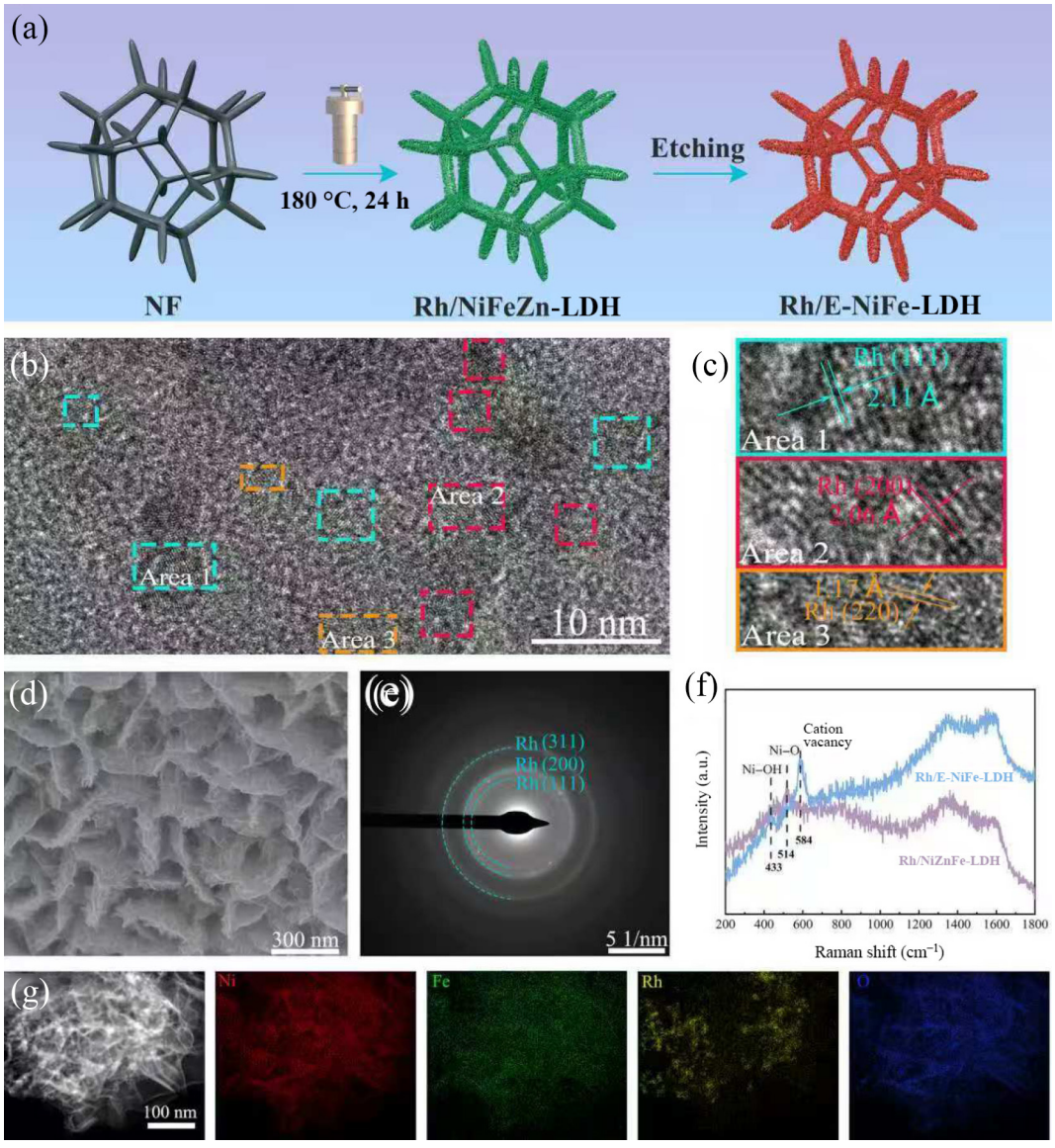

Figure 1 Synthesis and properties of Rh/E-NiFe-LDH catalysts. (a) The synthetic pathway schematic diagram. (b) The TEM image. (c) Enlarged view of the corresponding area. (d) The SEM image. (e) The SAED pattern. (f) Raman spectra of the samples. (g) The HR-TEM image and EDX elemental mapping images.

results demonstrate that this strategy is equally effective in the system for creating Ni vacancies, underscoring its broad applicability and reliability in defect engineering. Figure 1(g) demonstrates EDX elemental mapping images of Rh/E-NiFe-LDH, where Ni, Fe, Rh, and O are evenly distributed throughout the sample. Furthermore, SEM images and elemental mapping for the control samples are shown in Figs. S5–S8 in the ESM, revealing nanosheet morphology and homogeneous element distribution across all synthesized materials. ICP-OES measurements (Fig. S9 in the ESM) indicate that the Rh content in Rh/E-NiFe-LDH is 1.48 wt.%, higher than in the pre-etched samples. This suggests that the cation vacancies formed during etching play a role in stabilizing the Rh clusters [46, 47]. Furthermore, the absence of detectable Zn after etching confirms the complete removal of the zinc component. These results collectively confirm the successful fabrication of Rh/E-NiFe-LDH with well-dispersed Rh clusters and abundant cation vacancies, laying the foundation for its enhanced catalytic performance.

The chemical composition and electronic properties of Rh/E-NiFe-LDH and Rh/NiFe-LDH were thoroughly investigated using XPS measurement. As shown in Fig. 2(a), the survey spectra confirm the presence of Ni, Fe, O, Rh, and C in both samples. Carbon was used as a reference for energy calibration to accurately determine the binding energies of the elements (Fig. S10 in the ESM) [48]. Figure 2(b) presents the Ni 2p XPS spectra of Rh/E-NiFe-LDH and Rh/NiFe-LDH. The peaks at 855.58 and 873.28 eV correspond to the Ni $2p_{3/2}$ and Ni $2p_{1/2}$ states in Rh/E-NiFe-LDH, respectively, with satellite peaks observed at 861.56 and 879.54 eV. Compared to Rh/NiFe-LDH, the Ni 2p peaks in Rh/E-NiFe-LDH exhibit a negative shift of around −0.52 eV, demonstrating a decline in the average oxidation state of Ni in Rh/E-NiFe-LDH. The Ni^0 peak detected in Rh/NiFe-LDH may stem from the nickel foam substrate. The Fe 2p XPS spectra in Fig. 2(c) reveal a positive shift of 0.6 eV in Rh/E-NiFe-LDH after alkaline etching, which can be attributed to the formation of cationic defects. In Fig. 2(d), the absence of Zn-related signals in the Zn 2p XPS spectra of Rh/E-NiFe-LDH after alkaline etching further confirms the complete removal of Zn, consistent with the ICP analysis results. Figure 2(e)

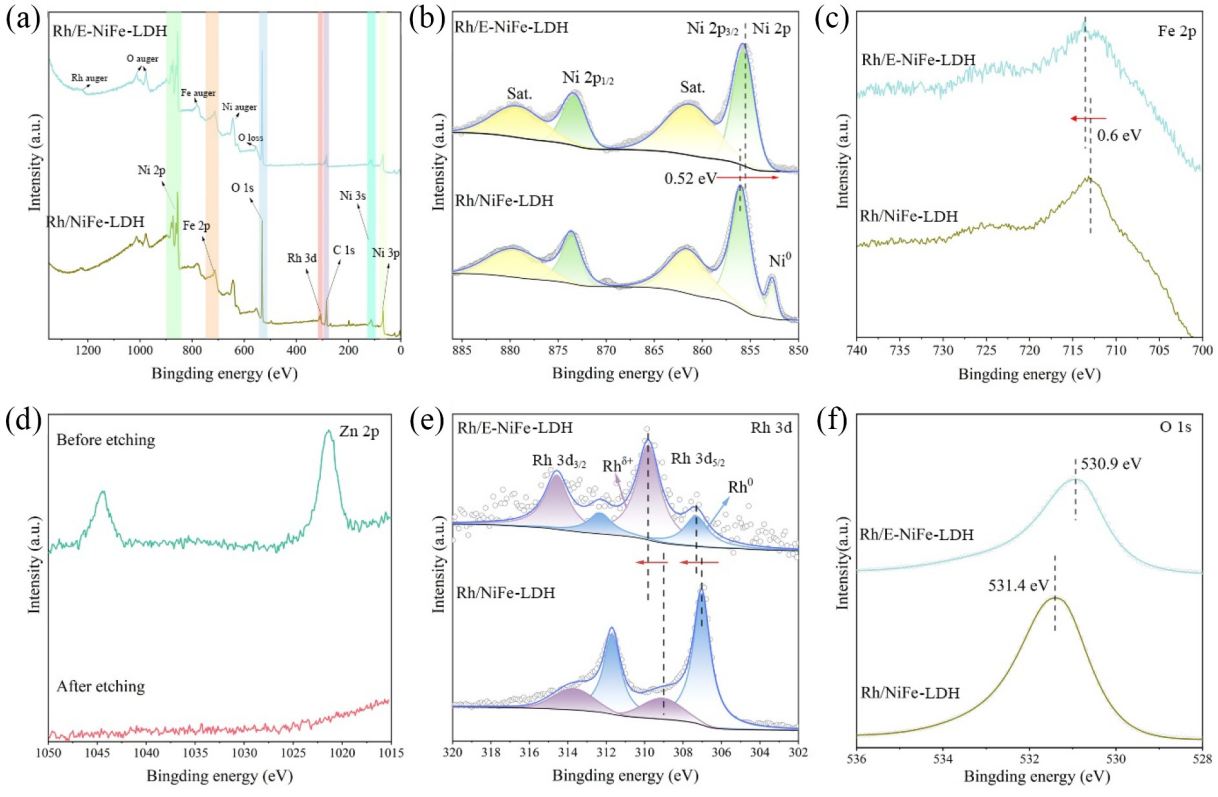

Figure 2 XPS spectra characterization s. (a) The samples' XPS survey spectra. ((b)–(f)) The samples' high-resolution XPS spectra: (b) Ni 2p; (c) Fe 2p; (d) Zn 2p; (e) Rh 3d; and (f) O1 s.

presents the Rh 3d XPS spectra for both Rh/E-NiFe-LDH and Rh/NiFe-LDH. These spectra are deconvoluted into Rh^0 and $Rh^{\delta+}$ peaks. In Rh/E-NiFe-LDH, the peaks at 307.32 and 312.32 eV correspond to the Rh^0 $3d_{5/2}$ and $3d_{3/2}$ states, respectively, while the peaks at 309.81 and 314.58 eV correspond to the $Rh^{\delta+}$ $3d_{5/2}$ and $3d_{3/2}$ states. Notably, compared to Rh/NiFe-LDH, both peaks in Rh/E-NiFe-LDH shift to higher binding energies, suggesting an increase in the oxidation state of Rh following the creation of cationic vacancies. Moreover, Table S1 in the ESM demonstrates that the $Rh^0/Rh^{\delta+}$ ratio decreases from 2.61 (for Rh/NiFe-LDH) to 0.32 (for Rh/E-NiFe-LDH), further confirming the higher oxidation state of Rh in Rh/E-NiFe-LDH. This result signifies that E-NiFe-LDH functions as an electron acceptor in this system. The O 1s XPS spectra are shown in Fig. 2(f). Compared to Rh/NiFe-LDH, the O 1s XPS spectra of Rh/E-NiFe-LDH exhibit a negative shift, suggesting that the Rh atoms in the clusters may coordinate with the O atoms in E-NiFe-LDH. This is due to the strong interaction between the Rh clusters and the defect-laden NiFe-LDH support [49]. The cationic defects facilitate electron transfer from Rh to E-NiFe-LDH via Rh–O bonding, altering the charge distribution of both the E-NiFe-LDH and Rh clusters.

3.2 Electrocatalytic performance for HER

The electrocatalytic HER performance of Rh/E-NiFe-LDH was examined in a 1.0 M KOH solution (pH = 14) using a standard three-electrode configuration. Comparative analyses of HER activities were conducted for NiFe-LDH, Rh/NiFe-LDH, and 20%Pt/C under identical conditions. As previously documented, NiFe-LDH exhibits limited HER kinetics in alkaline environments [50]. Figure 3(a) demonstrates that Rh/E-NiFe-LDH significantly enhances HER activity relative to NiFe-LDH, presenting the most effective polarization curve among the tested catalysts, with an onset potential approaching zero. Specifically, Rh/E-NiFe-LDH requires overpotentials of only 4 and 55 mV to achieve current densities of 10 and 100 $mA{\cdot}cm^{-2}$, respectively (Fig. 3(b)), outperforming Rh/NiFe-LDH (14 and 98 mV) and Pt/C (11 and 78 mV). When normalized by noble metal mass, Rh/E-NiFe-LDH achieves a mass activity of 9.57 $A{\cdot}mg^{-1}$, which is 25.7 times greater than that of Pt/C (0.37 $A{\cdot}mg^{-1}$) (Fig. S11 in the ESM). Moreover, the mass activity of Rh/E-NiFe-LDH is 2.19 times higher than that of Rh/NiFe-LDH (Fig. S11 in the ESM). This significant improvement highlights the enhanced catalytic efficiency of Rh/E-NiFe-LDH due to the optimized electronic structure and charge transfer properties induced by the etching process. Optimization of Rh loading reveals that 0.75 $mg{\cdot}mL^{-1}$ of rhodium chloride (1.48 wt.% Rh in the final product) yields optimal HER activity, with further increases or decreases in Rh content diminishing catalytic performance (Fig. S12 in the ESM). Comparative analysis with Rh/NiFeZn-LDH indicates that Rh/E-NiFe-LDH possesses markedly higher HER activity, underscoring the beneficial impact of cationic defects on NiFe-LDH performance and their enhanced interaction with Rh clusters (Fig. S13 in the ESM). The influence of alkaline etching duration on catalytic performance was also examined, with a 6 h treatment proving optimal (Fig. S14 in the ESM). Additionally, we explored the use of other noble metals, such as Ru, Ir, and Pt, using the same synthesis method. As shown in Fig. S15 in the ESM, the performance of these metals is inferior to that of Rh. Furthermore, we explored the effects of different alkali solutions, comparing potassium hydroxide (KOH) and sodium hydroxide (NaOH). As demonstrated in Fig. S16 in the ESM, the performance of the resulting products is nearly identical, suggesting that the type of alkali has a minimal impact. Furthermore, we

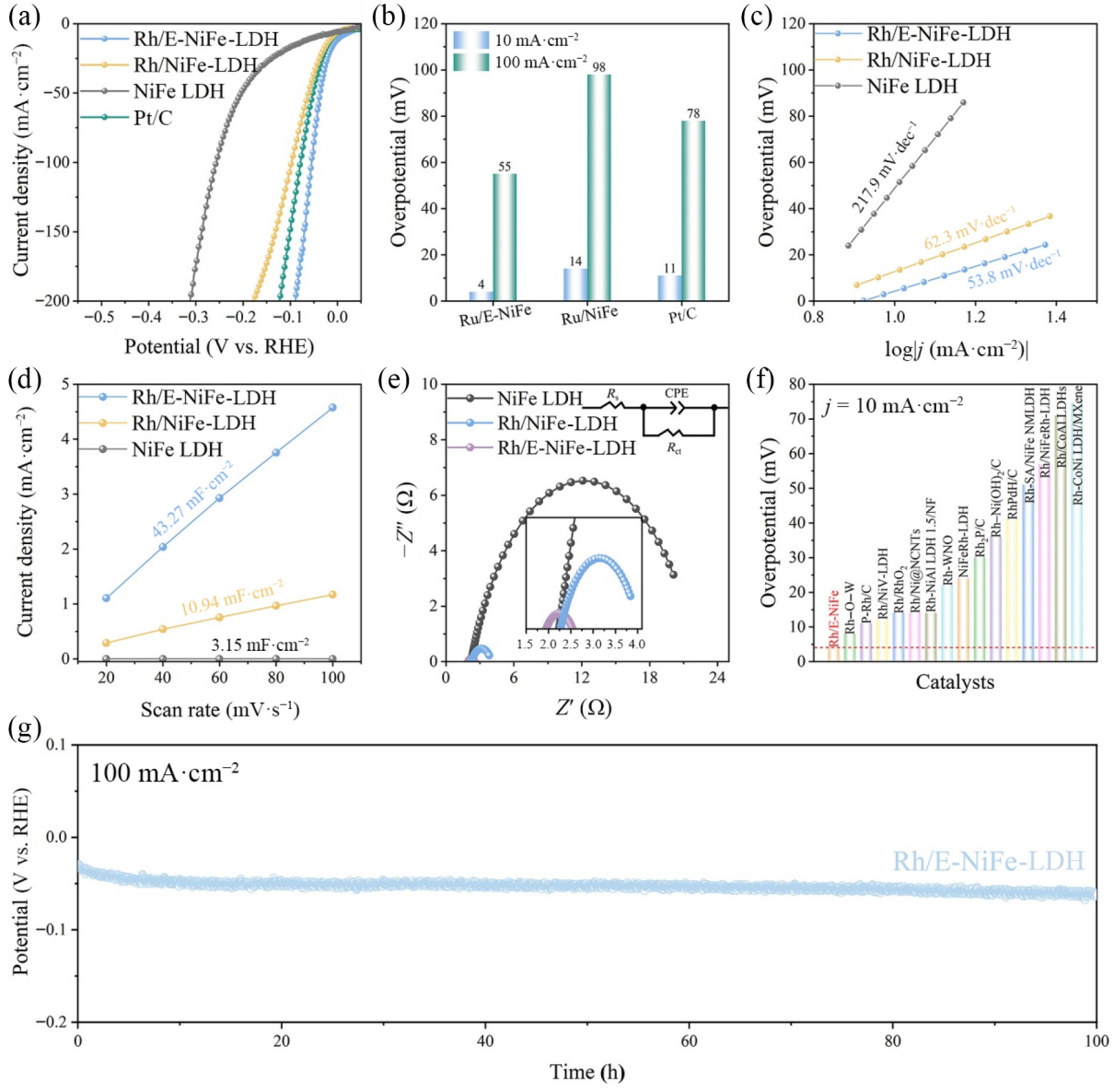

Figure 3 Electrocatalytic performance characterization. (a) HER polarization curves, (b) overpotentials, (c) Tafel slopes, (d) EIS spectra, and (e) C_{dl} of different catalysts. (f) Comparison of overpotentials. (g) 100 h HER stability test at 100 mA·cm^{-2}.

examined the influence of alkali concentration, as shown in Fig. S16 in the ESM, and found that a 5 M KOH solution provides the best results. The Tafel slope, derived from the polarization curve, provides information about the rate-determining step (RDS) of the HER mechanism. The Tafel slope for Rh/E-NiFe-LDH is 53.8 mV·dec^{-1}, which is lower than that of Rh/NiFe-LDH (62.3 mV·dec^{-1}) and NiFe-LDH (217.9 mV·dec^{-1}) (Fig. 3(c)). This suggests that the reaction follows the Volmer–Heyrovsky mechanism, with the recombination of adsorbed hydrogen as the RDS [51]. The electrochemical active surface area (ECSA) was determined using the double-layer capacitance approach within the non-Faradaic potential region [52]. The double-layer capacitance (C_{dl}) value of Rh/E-NiFe-LDH was found to be the highest at 43.27 mF·cm^{-2}, surpassing that of Rh/NiFe-LDH by 3.96 times and NiFe-LDH by 13.74 times (Fig. 3(d) and Fig. S17 in the ESM). This substantial increase in ECSA is attributed to the rougher surface morphology and the exposure of more active sites due to the tiny Rh clusters. To further clarify the contributions of the increased active surface area and intrinsic activity, we normalized the LSV curves by the ECSA, as shown in Fig. S18 in the ESM. The normalized current density of Rh/E-NiFe-LDH at −0.1 V is 7.92 mA·cm^{-2}, which is 4.55 times higher than that of Rh/NiFe-LDH. This indicates that the enhanced performance is not solely due to the increased active surface area but also reflects a significant improvement in intrinsic activity. EIS measurements were used to evaluate the charge transfer kinetics, employing a simplified Randles circuit model for fitting (Fig. 3(e)) [53]. The inset of Fig. 3(e) illustrates that the charge transfer resistance (R_{ct}) for Rh/E-NiFe-LDH is 0.53 Ω, significantly lower than that of the other electrocatalysts, indicating enhanced electron transfer kinetics for HER [54–57]. Considering the increased number of active sites and faster charge transfer, Rh/E-NiFe-LDH demonstrates the highest HER performance among the tested catalysts. Furthermore, its overpotential at 10 mA·cm^{-2} is lower than that of any other Rh-based catalysts reported to date (Fig. 3(f) and Table S2 in the ESM). Stability tests were performed on Rh/E-NiFe-LDH at a current

density of 100 mA·cm^{-2} to evaluate the catalyst's durability (Fig. 3(g)). The result shows that Rh/E-NiFe-LDH exhibits sustained stability for over 100 h, confirming the durability of its Rh-active sites under alkaline HER conditions, in contrast to other LDH-based catalysts (Table S2 in the ESM). Following the stability test, Rh/E-NiFe-LDH was characterised to assess any changes in its structure. The XRD patterns of the post-test sample exhibit identical nickel foam diffraction peaks as those observed prior to the test (Fig. S19 in the ESM). SEM analysis of the catalyst morphology reveals that it retains its nanosheet-like structure (Fig. S20 in the ESM). HR-TEM images further confirm that the Rh clusters remain intact after the electrochemical reaction (Fig. S21 in the ESM). XPS spectra of the post-test catalyst show negligible changes in the binding energies of Ni 2p, Fe 2p, and Rh 3d peaks, indicating minimal alteration of the catalyst's composition (Fig. S22 in the ESM). These findings demonstrate that Rh/E-NiFe-LDH exhibits excellent electrochemical stability.

3.3 DFT calculations

To investigate the cause of the enhanced HER activity of the Rh/E-NiFe-LDH catalyst, DFT calculations were performed. We constructed two sets of structural models: one for Rh clusters supported on NiFe-LDH (Rh/NiFe-LDH) and another for Rh clusters supported on NiFe-LDH with Ni defects (Rh/E-NiFe-LDH). For each model, we selected three crystallographic surfaces—(200), (111), and (220)—as the reaction surfaces, based on the exposed crystallographic facets identified through TEM images, as shown in Fig. 4(a) and Fig. S23 in the ESM. To model the Rh clusters, we employed a Rh_{13} cluster configuration, which is a widely adopted and representative model for metal clusters in Refs. [58, 59], as it effectively captures the electronic and structural properties of small metal clusters. We first calculated the density of states (DOS) for Rh/NiFe-LDH and Rh/E-NiFe-LDH. As shown in Figs. 4(b) and 4(c), the total DOS near the Fermi surface of Rh/E-NiFe-LDH is higher than that of Rh/NiFe-LDH, suggesting that the introduction of Ni defects enhances the electrical conductivity of the catalyst, which is beneficial for the catalytic reaction. In addition, the d-band center of the Rh clusters in Rh/E-NiFe-LDH is located at −1.632 eV, which is shifted negatively compared to the d-band center of the Rh clusters in Rh/NiFe-LDH, which is at

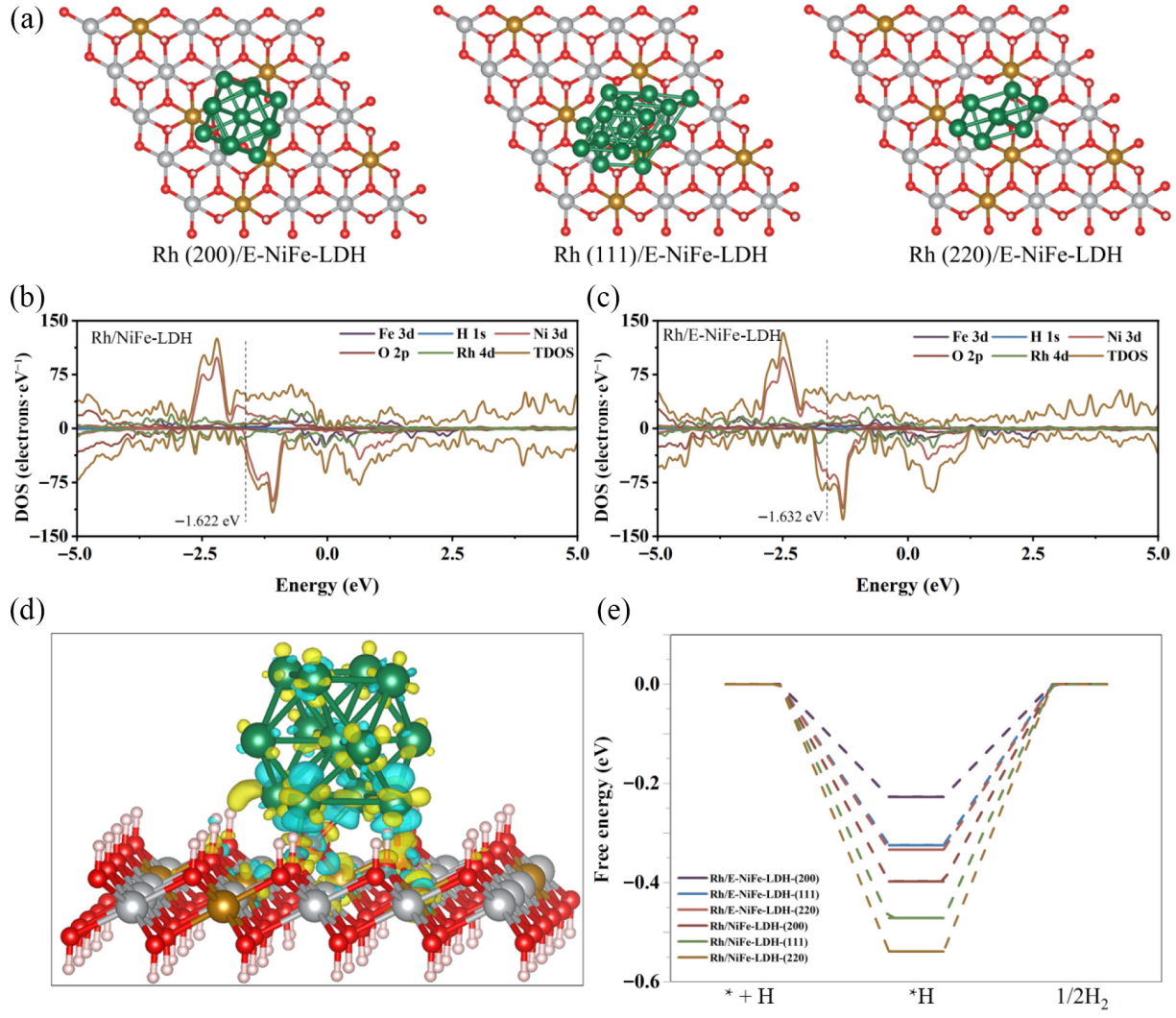

Figure 4 (a) Top view of structure model for Rh/E-NiFe-LDH with different exposed surface: left (200), middle (111), and right (220). The red, grey, brown, green, and white balls are O, Ni, Fe, Rh, and H atoms, respectively. (b) Projected DOS (PDOS) plots for Rh/NiFe-LDH. (c) PDOS plots for Rh/E-NiFe-LDH. (d) Charge density difference of Rh/E-NiFe-LDH (yellow: electron accumulation and cyan: electron depletion). (e) Adsorption free energies of H* on the surface of Rh/E-NiFe-LDH and Rh/NiFe-LDH.

−1.622 eV. The downward shift of the d-band center implies that the hydrogen adsorption on Rh is weakened, which promotes hydrogen desorption and thereby enhances HER activity [60]. We also calculated the differential charge density of Rh/E-NiFe-LDH. As shown in Fig. 4(d), significant charge transfer occurs at the interface between the Rh clusters and the NiFe-LDH support. The direction of this charge transfer is from Rh clusters to the carrier, which is consistent with the XPS results. To further understand the effect of Ni defects on charge transfer, we calculated the Bader charges of the Rh clusters in both Rh/NiFe-LDH and Rh/E-NiFe-LDH (Figs. S24 and S25 in the ESM). The Rh atoms in the clusters are either electron-rich or electron-deficient. Overall, after introducing Ni defects, the Rh clusters lose more electrons, indicating that Ni defects facilitate charge transfer between the Rh clusters and the support, which further corroborates the XPS results. The free energy of hydrogen adsorption (ΔG_H) is crucial for HER activity, with values closer to zero being indicative of better HER performance. We calculated the hydrogen adsorption free energy for the three crystal faces of both catalysts (Figs. S26 and S27 in the ESM). As shown in Fig. 4(e), for Rh/NiFe-LDH, the ΔG_H values for the (200), (111), and (220) surfaces are −0.398, −0.471, and −0.539 eV, respectively. These relatively large values suggest strong hydrogen adsorption, which is unfavorable for HER. In contrast, for Rh/E-NiFe-LDH, the ΔG_H values of these surfaces decrease to −0.227, −0.325, and −0.334, respectively, indicating weakened hydrogen adsorption. This reduction in hydrogen adsorption is consistent with the downward shift of the d-band center of Rh/E-NiFe-LDH. Overall, the results suggest that Ni defects enhance charge transfer between the Rh clusters and the support, shifting the d-band center of the Rh clusters. This weakening of hydrogen adsorption on the active crystal surfaces improves the HER performance of Rh/E-NiFe-LDH.

4 Conclusions

In conclusion, we successfully synthesized Rh clusters supported on cationic defect-rich NiFe-LDH through a facile solvothermal method followed by alkali etching. The Rh clusters feature multiple highly active crystalline facets, which significantly enhance catalytic activity. The introduced cationic defects facilitate efficient charge transfer between the Rh clusters and the NiFe-LDH support, optimizing both electrical conductivity and hydrogen adsorption properties. The resulting catalyst, with only 1.48 wt.% Rh loading achieves an exceptionally low overpotential under alkaline conditions, outperforming all previously reported Rh-based catalysts. DFT calculations reveal that the cationic defects induce a downward shift in the d-band center of Rh, weakening hydrogen adsorption and further improving catalytic performance. This study offers valuable insights for designing highly efficient alkaline HER catalysts with minimized noble metal usage.

Electronic Supplementary Material: Supplementary material (XRD patterns, SEM images, TEM images, EPR spectra, ICP-OES results, XPS spectra, LSV curves, CV sweeps, and calculation models) is available in the online version of this article at https://doi.org/10.26599/NR.2025.94907391.

Data availability

All data needed to support the conclusions in the paper are presented in the manuscript and the Electronic Supplementary Material. Additional data related to this paper may be requested from the corresponding author upon request.

Acknowledgements

This work was financially supported by the National Natural Science Foundation of China (Nos. 52072255, 52271184, and 52250402), Science Fund for Distinguished Young Scholars of Zhejiang Province (No. LR22E020003), Natural Science Foundation of Zhejiang Province (No. LY23E020001), and High-level Talents Special Support Program of Taizhou, and Science and Technology Plan Project of Taizhou (No. 24gyb14).

Declaration of competing interest

All the contributing authors report no conflict of interests in this work.

Author contribution statement

Q. A. L.: Conceptualization, methodology, investigation, data curation, visualization, formal analysis, writing – original draft. H. H. Z.: Investigation, validation. D. Y.: Investigation, validation, data curation. J. J. G.: Investigation, validation. L. L. Z.: Investigation, validation. L. G.: Supervision, funding acquisition, project administration, writing – review & editing. S. C. C.: Supervision, project administration. S. J. S: Supervision, experimental design, writing – review & editing. W. W. Z.: Supervision, funding acquisition, project administration, writing – review & editing. All the authors have approved the final manuscript.

Use of AI statement

None.

References

[1] Zhang, L. L.; Shi, X. X.; Xu, A. J.; Zhong, W. W.; Zhang, J. T.; Shen, S. J. Novel CoP/$CoMoP_2$ heterojunction with nanoporous structure as an efficient electrocatalyst for hydrogen evolution. *Nano Res.* **2024**, *17*, 3693–3699.

[2] Zhang, H. H.; Song, K.; Lin, Z. P.; Wang, Z. P.; Zhang, L. L.; Shen, S. J.; Gu, L.; Zhong, W. W. *In situ* reconstructed Ru clusters on $LaRuSi_3$ with enhanced electrocatalytic activity for alkaline hydrogen evolution. *Adv. Funct. Mater.* **2024**, *34*, 2405897.

[3] Song, K.; Zhang, H. H.; Lin, Z. P.; Wang, Z. P.; Zhang, L. L.; Shi, X. X.; Shen, S. J.; Chen, S. C.; Zhong, W. W. Interfacial engineering of cobalt thiophosphate with strain effect and modulated electron structure for boosting electrocatalytic hydrogen evolution reaction. *Adv. Funct. Mater.* **2024**, *34*, 2312672.

[4] Feidenhans'l, A. A.; Regmi, Y. N.; Wei, C.; Xia, D.; Kibsgaard, J.; King, L. A. Precious metal free hydrogen evolution catalyst design and application. *Chem. Rev.* **2024**, *124*, 5617–5667.

[5] Mu, X. Q.; Zhang, X. Y.; Chen, Z. Y.; Gao, Y.; Yu, M.; Chen, D.; Pan, H. Z.; Liu, S. L.; Wang, D. S.; Mu, S. C. Constructing symmetry-mismatched $Ru_xFe_{3-x}O_4$ heterointerface-supported Ru clusters for efficient hydrogen evolution and oxidation reactions. *Nano Lett.* **2024**, *24*, 1015–1023.

[6] Mu, X. Q.; Yuan, Y. T.; Yu, M.; Hu, Y. J.; Zeng, W. H.; Peng, W.; Zhang, Y. F.; Liu, X. Y.; Liu, S. L.; Mu, S. C. Robust water/seawater-electrolysis hydrogen production at industrial-scale current densities by modulating built-in-outer electric field of catalytic substance. *Nano Energy* **2024**, *131*, 110216.

[7] Esfandiari, N.; Aliofkhazraei, M.; Colli, A. N.; Walsh, F. C.; Cherevko, S.; Kibler, L. A.; Elnagar, M. M.; Lund, P. D.; Zhang, D.

K.; Omanovic, S. et al. Metal-based cathodes for hydrogen production by alkaline water electrolysis: Review of materials, degradation mechanism, and durability tests. *Prog. Mater. Sci.* **2024**, *144*, 101254.

[8] Zhang, Y. J.; Wang, X. K.; Song, X. J.; Jiang, H. Q. Collaborative effect between single-atom Re and S vacancy on modulating localized electronic structure of MoS_2 catalysts for alkaline hydrogen evolution. *Nano Res.* **2024**, *17*, 9507–9517.

[9] Tan, L.; Wang, H. F.; Qi, C. H.; Peng, X.; Pan, X. X.; Wu, X. T.; Wang, Z. K.; Ye, L.; Xiao, Q.; Luo, W. et al. Regulating Pt electronic properties on NiFe layered double hydroxide interface for highly efficient alkaline water splitting. *Appl. Catal. B: Environ.* **2024**, *342*, 123352.

[10] Shen, S. J.; Zhang, H. H.; Song, K.; Wang, Z. P.; Shang, T. T.; Gao, A.; Zhang, Q. H.; Gu, L.; Zhong, W. W. Multi-*d* electron synergy in $LaNi_{1-x}Co_xRu$ intermetallics boosts electrocatalytic hydrogen evolution. *Angew. Chem., Int. Ed.* **2024**, *63*, e202315340.

[11] Hou, M. Y.; Zheng, L. R.; Zhao, D.; Tan, X.; Feng, W. Y.; Fu, J. T.; Wei, T. X.; Cao, M. H.; Zhang, J. T.; Chen, C. Microenvironment reconstitution of highly active Ni single atoms on oxygen-incorporated Mo_2C for water splitting. *Nat. Commun.* **2024**, *15*, 1342.

[12] Santos, E.; Quaino, P.; Schmickler, W. Theory of electrocatalysis: Hydrogen evolution and more. *Phys. Chem. Chem. Phys.* **2012**, *14*, 11224–11233.

[13] Noerskov, J. K.; Bligaard, T.; Logadottir, A.; Kitchin, J. R.; Chen, J. G.; Pandelov, S.; Stimming, U. Trends in the exchange current for hydrogen evolution. *ChemInform* **2005**, *36*, J23–J26.

[14] Zhang, Y.; Mu, X. Q.; Liu, Z. Y.; Zhao, H. Y.; Zhuang, Z. C.; Zhang, Y. F.; Mu, S. C.; Liu, S. L.; Wang, D. S.; Dai, Z. H. Twin-distortion modulated ultra-low coordination PtRuNi–O_x catalyst for enhanced hydrogen production from chemical wastewater. *Nat. Commun.* **2024**, *15*, 10149.

[15] Yan, Z. X.; Liu, Z. R.; Zhou, G. S.; Jin, T. C.; Zhang, H. H.; Gu, L.; Gao, T.; Shen, S. J.; Zhong, W. W. Short-path hydrogen spillover on CeO_2-supported PtPd nanoclusters for efficient hydrogen evolution in acidic media. *Angew. Chem., Int. Ed.*, in press, DOI: 10.1002/anie.202501964.

[16] Li, M. T.; Zheng, X. Q.; Li, L.; Wei, Z. D. Research progress of hydrogen oxidation and hydrogen evolution reaction mechanism in alkaline media. *Acta Phys. Chim. Sin.* **2021**, *37*, 2007054.

[17] Wang, Y. F.; Luo, X.; Lu, W. J.; Yang, L.; Huang, B.; Li, P. T.; Yang, Y. Q. Carbon supported bifunctional Rh–$Ni(OH)_2$/C nanocomposite catalysts with high electrocatalytic efficiency for alkaline hydrogen evolution reaction. *Int. J. Hydrogen Energy* **2022**, *47*, 13674–13682.

[18] Zhang, K. X.; Chen, L.; Liu, Z. P. Do Rh-hydride phases contribute to the catalytic activity of Rh catalysts under reductive conditions. *J. Am. Chem. Soc.* **2024**, *146*, 35416–35426.

[19] Pan, S. Y.; Li, C.; Xiong, T. T.; Xie, Y. H.; Luo, F.; Yang, Z. H. Hydrogen spillover in MoO_xRh hierarchical nanosheets boosts alkaline HER catalytic activity. *Appl. Catal. B: Environ.* **2024**, *341*, 123275.

[20] Liu, Y. H.; Ding, J.; Li, F. H.; Su, X. Z.; Zhang, Q. T.; Guan, G. J.; Hu, F. X.; Zhang, J. C.; Wang, Q. L.; Jiang, Y. C. et al. Modulating hydrogen adsorption via charge transfer at the semiconductor–metal heterointerface for highly efficient hydrogen evolution catalysis. *Adv. Mater.* **2023**, *35*, 2207114.

[21] Sun, H. C.; Li, L. F.; Humayun, M.; Zhang, H. M.; Bo, Y. N.; Ao, X.; Xu, X. F.; Chen, K.; Ostrikov, K.; Huo, K. F. et al. Achieving highly efficient pH-universal hydrogen evolution by superhydrophilic amorphous/crystalline $Rh(OH)_3$/NiTe coaxial nanorod array electrode. *Appl. Catal. B: Environ.* **2022**, *305*, 121088.

[22] Zhong, W. W.; Xiao, B. B.; Lin, Z. P.; Wang, Z. P.; Huang, L. A.; Shen, S. J.; Zhang, Q. H.; Gu, L. $RhSe_2$: A superior 3D electrocatalyst with multiple active facets for hydrogen evolution reaction in both acid and alkaline solutions. *Adv. Mater.* **2021**, *33*, 2007894.

[23] Zheng, Y. J.; Zhang, B.; Ma, T.; Yan, R.; Geng, W.; Zeng, Z. Y.; Zhang, Y. N.; Li, S. Nitrided rhodium nanoclusters with optimized water bonding and splitting effects for pH-universal H_2-production. *Small* **2024**, *20*, 2307405.

[24] Logeshwaran, N.; Kim, G.; Thangavel, P.; Jeon, S. S.; Thiyagarajan, K.; Kishore, K. R.; Lee, H.; Seo, I.; Yun, H.; Lee, S. et al. Synergistic configuration of binary rhodium single atoms in carbon nanofibers for high-performance alkaline water electrolyzer. *Adv. Sci.* **2025**, *12*, 2413176.

[25] Chen, X. J.; Li, W. M.; Wang, C.; Lu, X. F. Wet chemical synthesis of rhodium nanoparticles anchored on cobalt/nitrogen-doped carbon nanofibers for high-performance alkaline and acidic hydrogen evolution. *J. Colloid Interface Sci.* **2023**, *650*, 304–312.

[26] Wang, Y. H.; Li, S. Q.; Hou, X.; Cui, T. T.; Zhuang, Z. C.; Zhao, Y. H.; Wang, H. Z.; Wei, W.; Xu, M.; Fu, Q. et al. Low-spin Fe^{3+} evoked by multiple defects with optimal intermediate adsorption attaining unparalleled performance in water oxidation. *Adv. Mater.* **2024**, *36*, 2412598.

[27] Lei, H.; Wan, Q. X.; Tan, S. Z.; Wang, Z. L.; Mai, W. J. Pt-quantum-dot-modified sulfur-doped NiFe layered double hydroxide for high-current-density alkaline water splitting at industrial temperature. *Adv. Mater.* **2023**, *35*, 2208209.

[28] Huo, J. M.; Ma, Z. L.; Wang, Y.; Cao, Y. J.; Jiang, Y. C.; Li, S. N.; Chen, Y.; Hu, M. C.; Zhai, Q. G. Monodispersed Pt sites supported on NiFe-LDH from synchronous anchoring and reduction for high efficiency overall water splitting. *Small* **2023**, *19*, 2207044.

[29] Wang, W.; Liu, Y. C.; Chen, S. L. Use of NiFe layered double hydroxide as electrocatalyst in oxygen evolution reaction: Catalytic mechanisms, electrode design, and durability. *Acta Phys. Chim. Sin.* **2024**, *40*, 2303059.

[30] Shen, S. J.; Li, Q. A.; Zhang, H. H.; Yang, D.; Gong, J. J.; Gu, L.; Gao, T.; Zhong, W. W. Negative-valent platinum stabilized by Pt–Ni electron bridges on oxygen-deficient NiFe-LDH for enhanced electrocatalytic hydrogen evolution. *Adv. Mater.*, in press, DOI: 10.1002/adma.202500595.

[31] Wu, Y. W.; Chen, M. P.; Sun, H. C.; Zhou, T.; Chen, X. Q.; Na, G. H.; Qiu, G. Y.; Li, D. Q.; Yang, N.; Zheng, H. S. et al. Coupling Ir single atom with NiFe LDH/NiMo heterointerface toward efficient and durable water splitting at large current density. *Appl. Catal. B: Environ. Energy* **2025**, *360*, 124548.

[32] Zhu, Y.; Chen, Y. X.; Feng, Y. F.; Meng, X. M.; Xia, J.; Zhang, G. Q. Constructing Ru–O–TM bridge in NiFe-LDH enables high current hydrazine-assisted H_2 production. *Adv. Mater.* **2024**, *36*, 2401694.

[33] Chen, Y.; Liu, Y. D.; Zhai, W. F.; Liu, H.; Sakthivel, T.; Guo, S. W.; Dai, Z. F. Metastabilizing the ruthenium clusters by interfacial oxygen vacancies for boosted water splitting electrocatalysis. *Adv. Energy Mater.* **2024**, *14*, 2400059.

[34] Yan, L.; Song, D.; Liang, J. Y.; Li, X. Y.; Li, H.; Liu, Q. B. Fabrication of highly efficient Rh-doped cobalt-nickel-layered double hydroxide/MXene-based electrocatalyst with rich oxygen vacancies for hydrogen evolution. *J. Colloid Interface Sci.* **2023**, *640*, 338–347.

[35] Li, Y. J.; Wang, X.; Han, X.; Yin, S.; Xia, J. X. Assembly engineering of Rh atoms on CoAl-layered double hydroxide nanosheets for boosting alkaline water splitting. *ACS Appl. Nano Mater.* **2023**, *6*, 7984–7991.

[36] Fan, B. B.; Wang, H. Z.; Han, X. P.; Deng, Y. D.; Hu, W. B. Single atoms (Pt, Ir, and Rh) anchored on activated NiCo LDH for alkaline hydrogen evolution reaction. *Chem. Commun.* **2022**, *58*, 8254–8257.

[37] Zhang, B. W.; Zhu, C. Q.; Wu, Z. S.; Stavitski, E.; Lui, Y. H.; Kim, T. H.; Liu, H.; Huang, L.; Luan, X. C.; Zhou, L. et al. Integrating Rh species with NiFe-layered double hydroxide for overall water splitting. *Nano Lett.* **2020**, *20*, 136–144.

[38] Zhang, Y.; Li, G.; Zhao, Z. L.; Han, L. L.; Feng, Y. G.; Liu, S. H.; Xu, B. Y.; Liao, H. G.; Lu, G.; Xin, H. L. et al. Atomically isolated Rh sites within highly branched Rh_2Sb nanostructures enhance bifunctional hydrogen electrocatalysis. *Adv. Mater.* **2021**, *33*, 2105049.

[39] Sun, Z. J.; Yang, J. L.; Xu, H. F.; Jiang, C. L.; Niu, Y. X.; Lian, X.;

Liu, Y.; Su, R. Q.; Liu, D. Y.; Long, Y. et al. Enabling an inorganic-rich interface via cationic surfactant for high-performance lithium metal batteries. *Nano-Micro Lett.* **2024**, *16*, 141.

[40] Park, H. K.; Ahn, H.; Lee, T. H.; Lee, J. Y.; Lee, M. G.; Lee, S. A.; Yang, J. W.; Kim, S. J.; Ahn, S. H.; Kim, S. Y. et al. Grain boundaries boost oxygen evolution reaction in NiFe electrocatalysts. *Small Methods* **2021**, *5*, 2000755.

[41] He, Y. M.; Tang, P. Y.; Hu, Z. L.; He, Q. Y.; Zhu, C.; Wang, L. Q.; Zeng, Q. S.; Golani, P.; Gao, G. H.; Fu, W. et al. Engineering grain boundaries at the 2D limit for the hydrogen evolution reaction. *Nat. Commun.* **2020**, *11*, 57.

[42] Peng, L. S.; Yang, N.; Yang, Y. Q.; Wang, Q.; Xie, X. Y.; Sun-Waterhouse, D.; Shang, L.; Zhang, T. R.; Waterhouse, G. I. N. Atomic cation-vacancy engineering of NiFe-layered double hydroxides for improved activity and stability towards the oxygen evolution reaction. *Angew. Chem., Int. Ed.* **2021**, *60*, 24612–24619.

[43] Xie, Q. X.; Cai, Z.; Li, P. S.; Zhou, D. J.; Bi, Y. M.; Xiong, X. Y.; Hu, E. Y.; Li, Y. P.; Kuang, Y.; Sun, X. M. Layered double hydroxides with atomic-scale defects for superior electrocatalysis. *Nano Res.* **2018**, *11*, 4524–4534.

[44] Liu, W.; Yu, J. G.; Li, T. S.; Li, S. H.; Ding, B. Y.; Guo, X. L.; Cao, A. Q.; Sha, Q. H.; Zhou, D. J.; Kuang, Y. et al. Self-protecting CoFeAl-layered double hydroxides enable stable and efficient brine oxidation at 2 $A \cdot cm^{-2}$. *Nat. Commun.* **2024**, *15*, 4712.

[45] Zeng, L. Y.; Chen, Y. J.; Sun, M. Z.; Huang, Q. Z.; Sun, K. A.; Ma, J. Y.; Li, J.; Tan, H.; Li, M. G.; Pan, Y. et al. Cooperative Rh–O_5/Ni(Fe) site for efficient biomass upgrading coupled with H_2 production. *J. Am. Chem. Soc.* **2023**, *145*, 17577–17587.

[46] Cai, D. X.; Zhang, J.; Kong, Z.; Li, Z. S. Synergistic effect of single-atom catalysts and vacancies of support for versatile catalytic applications. *ChemCatChem* **2024**, *16*, e202301414.

[47] Wang, L. M.; Zhang, L. L.; Ma, W.; Wan, H.; Zhang, X. J.; Zhang, X.; Jiang, S. Y.; Zheng, J. Y.; Zhou, Z. *In situ* anchoring massive isolated Pt atoms at cationic vacancies of α-$Ni_xFe_{1-x}(OH)_2$ to regulate the electronic structure for overall water splitting. *Adv. Funct. Mater.* **2022**, *32*, 2203342.

[48] Song, K.; Yang, D.; Zhou, C. J.; Li, Q. A.; Zhang, L. L.; Gong, J. J.; Zhong, W. W.; Shen, S. J.; Chen, S. C. CoPS/Co_4S_3 heterojunction with highly exposed active sites and dual-site synergy for effective hydrogen evolution reactions. *Chem.—Eur. J.* **2024**, *30*, e202401038.

[49] Zhai, P. L.; Xia, M. Y.; Wu, Y. Z.; Zhang, G. H.; Gao, J. F.; Zhang, B.; Cao, S. Y.; Zhang, Y. T.; Li, Z. W.; Fan, Z. Z. et al. Engineering single-atomic ruthenium catalytic sites on defective nickel-iron layered double hydroxide for overall water splitting. *Nat. Commun.* **2021**, *12*, 4587.

[50] Li, X. P.; Zheng, L. R.; Liu, S. J.; Ouyang, T.; Ye, S. Y.; Liu, Z. Q. Heterostructures of NiFe LDH hierarchically assembled on MoS_2 nanosheets as high-efficiency electrocatalysts for overall water splitting. *Chin. Chem. Lett.* **2022**, *33*, 4761–4765.

[51] Chen, G. B.; Wang, T.; Zhang, J.; Liu, P.; Sun, H. J.; Zhuang, X. D.; Chen, M. W.; Feng, X. L. Accelerated hydrogen evolution kinetics on NiFe-layered double hydroxide electrocatalysts by tailoring water dissociation active sites. *Adv. Mater.* **2018**, *30*, 1706279.

[52] Zhang, T. Y.; Jin, J.; Chen, J. M.; Fang, Y. Y.; Han, X.; Chen, J. Y.; Li, Y. P.; Wang, Y.; Liu, J. F.; Wang, L. Pinpointing the axial ligand effect on platinum single-atom-catalyst towards efficient alkaline hydrogen evolution reaction. *Nat. Commun.* **2022**, *13*, 6875.

[53] Wang, Y. Y.; Zhang, Y. Q.; Liu, Z. J.; Xie, C.; Feng, S.; Liu, D. D.; Shao, M. F.; Wang, S. Y. Layered double hydroxide nanosheets with multiple vacancies obtained by dry exfoliation as highly efficient oxygen evolution electrocatalysts. *Angew. Chem., Int. Ed.* **2017**, *56*, 5867–5871.

[54] Jin, T. C.; Shen, S. J.; Xu, A. J.; Pan, J. Q.; Zhou, G. S.; Zhong, W. W. Triggering intrinsic electrochemical hydrogen evolution activity within heusler alloys via electronegativity-induced charge rearrangement. *Small*, in press, DOI: 10.1002/smll.202500667.

[55] Mu, X. Q.; Liu, S. L.; Zhang, M. Y.; Zhuang, Z. C.; Chen, D.; Liao, Y. R.; Zhao, H. Y.; Mu, S. C.; Wang, D. S.; Dai, Z. H. Symmetry-broken Ru nanoparticles with parasitic Ru–Co dual-single atoms overcome the Volmer step of alkaline hydrogen oxidation. *Angew. Chem., Int. Ed.* **2024**, *63*, e202319618.

[56] Chao, T. T.; Xie, W. B.; Hu, Y. M.; Yu, G.; Zhao, T. H.; Chen, C.; Zhang, Z. D.; Hong, X.; Jin, H. L.; Wang, D. S. et al. Reversible hydrogen spillover at the atomic interface for efficient alkaline hydrogen evolution. *Energy Environ. Sci.* **2024**, *17*, 1397–1406.

[57] Hu, Y. M.; Chao, T. T.; Li, Y. P.; Liu, P. G.; Zhao, T. H.; Yu, G.; Chen, C.; Liang, X.; Jin, H. L.; Niu, S. W. et al. Cooperative Ni(Co)–Ru–P sites activate dehydrogenation for hydrazine oxidation assisting self-powered H_2 production. *Angew. Chem., Int. Ed.* **2023**, *62*, e202308800.

[58] Lustemberg, P. G.; Mao, Z. T.; Salcedo, A.; Irigoyen, B.; Ganduglia-Pirovano, M. V.; Campbell, C. T. Nature of the active sites on Ni/CeO_2 catalysts for methane conversions. *ACS Catal.* **2021**, *11*, 10604–10613.

[59] Schleder, G. R.; Fazzio, A.; Arantes, J. T. Oxidation of Ni_{13} clusters. *Int. J. Quantum Chem.* **2019**, *119*, e25874.

[60] Wang, Z. Z.; Shen, S. J.; Wang, J. C.; Zhong, W. W. Modulating the *d*-band center of electrocatalysts for enhanced water splitting. *Chem.—Eur. J.* **2024**, *30*, e202402725.